Aerospace Science and Technology 23 (2012) 296–304

Contents lists available at SciVerse ScienceDirect

Aerospace Science and Technology

www.elsevier.com/locate/aescte

# Numerical simulation of ice accretions on an aircraft wing

Yihua Cao [a,*], Chao Ma [a], Qiang Zhang [a], John Sheridan [b]

[a] School of Aeronautic Science and Engineering, Beijing University of Aeronautics and Astronautics, Beijing, China
[b] Department of Mechanical & Aerospace Engineering, Faculty of Engineering, Monash University, Australia

ARTICLE INFO

*Article history:*
Received 19 September 2008
Received in revised form 25 March 2011
Accepted 18 August 2011
Available online 25 August 2011

*Keywords:*
Ice accretion
Two-phase flows
Collection efficiency
Roughness
Numerical simulation

ABSTRACT

An approach based on the Eulerian two-phase flow theory to numerically simulate ice accretions on an aircraft wing is developed. The air flowfield is obtained through Euler flow computation. The water droplets' flowfield is solved through proposing a permeable wall to simulate the droplets impingement. The droplets collection efficiency is calculated according to the droplets velocity and apparent density distribution. The thermodynamic model of ice accretion is based on the classical Messinger model and an integral boundary layer method is employed to account for roughness effect in calculating the convective heat transfer coefficient. The ice shape is built with the assumption that ice grows in the direction normal to the airfoil/wing surface. The ice accretions on a NACA0012 airfoil and a GLC-305 wing model under different icing conditions are evaluated and the comparison between the predicted results and experimental data indicates that the simulation approach developed in this paper is feasible and effective.


## 1. Introduction

Ice accretion on aircraft wings can be a hazard to flight safety. The cause of the accretion is due to supercooled water droplets impinging to the windward face of the wings. Ice accretions may modify the designed aerodynamic shapes and considerably degrade the aerodynamic performances. Thus, being able to evaluate the mechanisms and consequences of the ice accretion is of great importance to anti-icing and de-icing.

Different icing conditions form different types of ice accretions. Depending on the icing mechanism, ice accretions can be classified as: rime ice, glaze ice and mixed ice. Rime ice usually occurs in low velocity, low environment temperature and low liquid water content and forms because supercooled droplets freeze immediately when they impinge onto the wing surface. The glaze ice forms at an environment temperature around 0 °C and a high liquid water content [11]. The droplets freeze partially at impingement location and then freeze gradually during the flow along the wing surface caused by airflow. The mixed ice is defined as a mixture of the rime ice and glaze ice. Glaze ice and mixed ice can corrupt the designed aerodynamic shapes of the wings more significantly than rime ice.

These forms of ice accretion can be investigated by several means, including flight tests, experimental simulation [1,13], engineering methods [4,17] and numerical simulation [16,15]. Flight test and experimental simulation can obtain exact ice shapes but are usually too expensive to be widely adopted. The engineering method uses the typical experimental data and empirical formulae but could hardly analyze the ice accretion process. Therefore, numerical simulation is widely adopted because it is economical and can simulate the icing process and so provide a relatively exact evaluation of ice accretion. Several codes for simulating ice accretion have been developed internationally, such as: LEWICE (USA) [12], CAPTA (France) [6], TRAJICE2 (UK) [5], FENSAP-ICE (Canada) [2], MULTIICE (Italy) [10,7].

Generally, the numerical simulation of ice accretion mainly consists of four modules: (1) air flowfield solution, (2) droplets collection efficiency calculation, (3) boundary layer characteristics evaluation, and (4) ice amount evaluation via thermodynamic model.

The air flowfield can be obtained by using the panel method, to solve the potential flow equation, or to solve the Euler equations or directly to solve Navier–Stokes equations. For example, the potential flow equation is solved in LEWICE, MULTIICE and TRAJICE2 codes while the Euler equations and N-S equations are solved in CAPTA and FENSAP-ICE codes respectively.

The droplets' collection efficiency on the wing surface is important in numerically simulating ice accretions and two computational methods are available: Lagrangian method and Eulerian two-phase flow method. The Lagrangian method obtains the collection efficiency by solving the motion equation of droplets to track each droplet's trajectory in the flowfield. Eulerian two-phase flow method considers the droplets in the airflow as a form of pseudo fluid [18] which interpenetrates with the air and the collection efficiency is obtained through solving the velocity and apparent density distribution of droplets. There are advantages in using the Eulerian two-phase flow method compared with a Lagrangian

* Correspondence to: Institute of Aircraft Design, Beijing University of Aeronautics & Astronautics, Beijing 100191, PR China.
*E-mail address:* yihuacs@yahoo.com.cn (Y. Cao).

1270-9638/$ – see front matter 
doi:10.1016/j.ast.2011.08.004

approach since the same mesh can be used to solve the governing equations for the airflow and droplets. Moreover, droplets' collection efficiency may be calculated through the solution of droplets' flowfield directly, which is significant to the investigation of ice accretions in three-dimensional application. The Eulerian two-phase flow method is employed in FENSAP-ICE code while the Lagrange approach is employed in the other codes.

The convective heat transfer coefficient is an essential parameter in the thermodynamic process of ice accretions. It primarily depends on the boundary layer properties, such as momentum thickness, skin friction coefficient and etc. FENSAP-ICE code solves the RANS equations and a modification is made to account for the roughness effect in one-equation turbulent model. The convective heat transfer coefficient is obtained through the temperature distribution near the wing surface. LEWICE, TRAJICE2 and MULTIICE codes employ integral boundary layer methods corrected to account for the roughness effect. In CAPTA code, the modification to roughness is added in the mixing length model to compute the convective heat transfer coefficient. The thermodynamic models in these ice accretion codes are mostly based on the classical Messinger model [8].

This paper presents a method to numerically simulate the ice accretions based on Eulerian two-phase flow theory. In two-dimensional application, the rime ice accretion, glaze ice accretion and mixed ice accretion are simulated with the following procedures: The air flowfield is obtained through solving Eulerian equations. A permeable wall is proposed to simulate the droplet impingement on an airfoil. The droplet collection efficiency can be obtained from the solution of the droplet flowfield. The convective heat transfer coefficient is evaluated through employing an integral boundary layer method corrected to account for roughness effect and the ice amount is evaluated through performing the mass and energy balances in the thermodynamic model. The process of ice accretion is simulated with the assumption that ice accumulates layer-by-layer and the ice shape is predicted with the assumption that ice grows in the direction normal to the airfoil surface. In three-dimensional application, the droplet impingement on a wing is simulated with the method adapted from the two-dimensional application, and then the three-dimensional rime ice accretions on a wing is obtained under the assumption that the droplets freeze immediately when they impinge onto the wing surface in an environment with very low temperature.

## 2. Governing equations of two-phase flows

The following assumptions are needed before the governing equations of two-phase flows are established:

(1) The volume fraction of droplets is so small that the effect of droplet movement on airflow can be neglected;
(2) The external forces imposed on the droplets only involve the drag, arising from airflow, gravity and buoyancy. The turbulent fluctuations of the airflow have no effect on the droplet movement;
(3) There is no heat transfer or evaporation in the movement of droplets before they impinge onto the wing. Thus, the physical parameters of the droplets are assumed not to be changed.
(4) The droplets are simplified to be spheres with a median volumetric diameter.
(5) After the droplets impinge onto the wing surface, they do not bounce and splash.

### 2.1. Solution of the governing equations for airflow

According to Assumption 1, there is no coupling relationship between the governing equations for airflow and the ones for droplets. Therefore, the governing equations for airflow can be solved independently. The panel method can calculate the air velocity at any point in the flowfield directly but usually lacks accuracy in computing the complete flowfield. In contrast, the solution of the Navier–Stokes equations can provide a more accurate flowfield computation but is time consuming. In order to synthetically consider the computational precision and efficiency, an Euler flow computation is adopted in this paper.

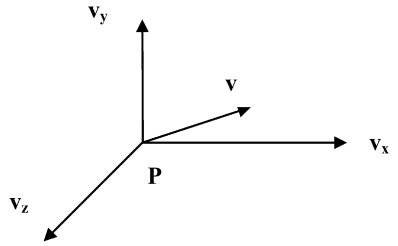


**Fig. 1.** The droplet velocity components.

### 2.2. Governing equations for droplets

Based on the Multi-fluid model of droplets [18], the droplets distributed in the flowfield can be regarded as a kind of pseudo fluid that penetrates the 'real' fluid in Eulerian coordinates. According to Assumptions 2, 3 and 4, the fluctuation term, phase-change term and Magnus force in the governing equations for droplets can be neglected. Furthermore, the energy equation needs not to be solved.

Therefore, the continuity and momentum equations for droplets in three-dimensional application can be simplified as:

$$\frac{\partial \bar{\rho}}{\partial t} + \frac{\partial(\bar{\rho} v_x)}{\partial x} + \frac{\partial(\bar{\rho} v_y)}{\partial y} + \frac{\partial(\bar{\rho} v_z)}{\partial z} = 0 \tag{1}$$

$$\frac{\partial(\bar{\rho} v_x)}{\partial t} + \frac{\partial(\bar{\rho} v_x v_x)}{\partial x} + \frac{\partial(\bar{\rho} v_y v_x)}{\partial y} + \frac{\partial(\bar{\rho} v_z v_x)}{\partial z} = F_{Dx} \tag{2}$$

$$\frac{\partial(\bar{\rho} v_y)}{\partial t} + \frac{\partial(\bar{\rho} v_x v_y)}{\partial x} + \frac{\partial(\bar{\rho} v_y v_y)}{\partial y} + \frac{\partial(\bar{\rho} v_z v_y)}{\partial z} = F_{Dy} + F_{GB} \tag{3}$$

$$\frac{\partial(\bar{\rho} v_z)}{\partial t} + \frac{\partial(\bar{\rho} v_x v_z)}{\partial x} + \frac{\partial(\bar{\rho} v_y v_z)}{\partial y} + \frac{\partial(\bar{\rho} v_z v_z)}{\partial z} = F_{Dz} \tag{4}$$

In above equations, $\bar{\rho}$ denotes droplet apparent density (i.e. the mass of droplets per unit volume) and $\bar{\rho} = \alpha_V \cdot \rho_W$, where $\alpha_V$, $\rho_W$ denote the droplet volume fraction and density of water, respectively. The symbols $v_x$, $v_y$, $v_z$ denote the droplet velocity components, as shown in Fig. 1.

The symbols $F_{Dx}$, $F_{Dy}$, $F_{Dz}$ denote the drag components caused by airflow and the symbol $F_{GB}$ denotes the resultant force of the gravity and buoyancy of droplets.

The formulae for calculating $F_{Dx}$, $F_{Dy}$, $F_{Dz}$ can be written as:

$$F_{Dx} = \frac{0.75\bar{\rho} \cdot C_D Re_d \cdot \mu}{\rho_w \cdot MVD^2}(u_x - v_x) \tag{5}$$

$$F_{Dy} = \frac{0.75\bar{\rho} \cdot C_D Re_d \cdot \mu}{\rho_w \cdot MVD^2}(u_y - v_y) \tag{6}$$

$$F_{Dz} = \frac{0.75\bar{\rho} \cdot C_D Re_d \cdot \mu}{\rho_w \cdot MVD^2}(u_z - v_z) \tag{7}$$

where, the symbols $u_x$, $u_y$, $u_z$ denote the air velocity components and the symbols $\mu$, $MVD$, $C_D$, $Re_d$ denote the air molecular viscosity coefficient, median volumetric diameter, drag coefficient and Reynolds number of the droplets, respectively. The expression of $Re_d$ can be written as:

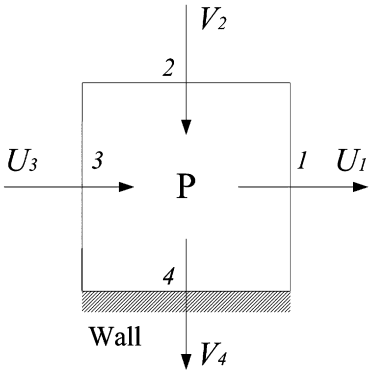


**Fig. 2.** Contravariant velocity distribution of the control volume for 2-D application.

$$Re_d = \frac{\rho_a \cdot MVD}{\mu}|u - v| \tag{8}$$

Furthermore, the combined variable $C_D Re_d$ can be calculated with the following formula [15]:

$$C_D Re_d = 24\left(1 + 0.197 Re_d^{0.63} + 2.6 \times 10^{-4} Re_d^{1.38}\right) \tag{9}$$

The formula calculating $F_{GB}$ can be written as:

$$F_{GB} = \bar{\rho} \cdot g \cdot (1 - \rho_a/\rho_w) \tag{10}$$

where $g$ is the acceleration due to gravity.

### 2.3. Simulation of droplet impingement on an airfoil/wing surface through a permeable wall

In the Eulerian two-phase flow method, the droplet collection efficiency is determined by the droplet apparent density and velocity near the wall. Therefore, the setting of the wall condition is an important factor in the solution of the droplet flowfield. Some previous literatures [2,3] set the initial values of the droplet apparent density and velocity near the wall to be zero, and no special techniques were employed to deal with the wall boundary. This might cause oscillations in the solution of the droplet flowfield and some extra stabilization terms must be added.

The approach taken in this paper is to use a permeable wall to simulate droplet impingement on an airfoil/wing surface. First, Cartesian coordinates are transformed into body-fitted curvilinear coordinates. In two-dimensional application, a control volume near the stagnation point of the airfoil is selected as the investigated object, as shown in Fig. 2.

From Fig. 2, the control volume has four interfaces with corresponding droplet velocities. These velocities are contravariant velocities in body-fitted curvilinear coordinates and they are perpendicular to corresponding interfaces. The contravariant velocities $U_1$ and $U_3$ in interface *1* and interface *3* are parallel to the wall boundary. Therefore, they do not contribute to the impingement. On the other hand, the contravariant velocity $V_2$ in interface *2* points to the interior of the control volume, which means that droplets will flow into the control volume through interface *2*.

If the droplet velocity on the wall boundary (which is a superposition to interface *4* of the control volume) is set to be zero, the droplet contravariant velocity $V_4$ is equal to zero. Therefore, in the discretization process using the finite-volume method, this setting is equivalent to a fact that droplets have no impingement with the wall because the net flux of droplets into interface *4* (namely the wall boundary) is null. As a result, most of the droplets which flow into the control volume through interface *2* settle in the control volume and cannot reach the wall. In this way the method cannot simulate the physical phenomenon of the impingement between the droplets and wall effectively. In fact, because of the means of the impingement between the droplets and wall, the supercooled droplets adhere to the wall after they have inelastic impingements with the wall. However, before the droplets reach the wall, they have fairly high normal velocity relative to the wall and this velocity turns into zero instantaneously when the droplets impinge with the wall inelastically.

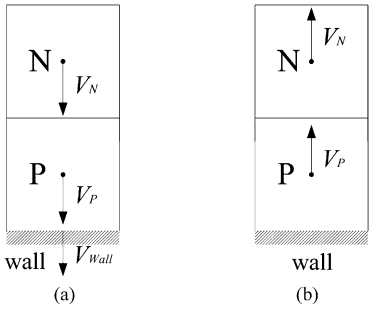


**Fig. 3.** Setting of the wall boundary conditions.

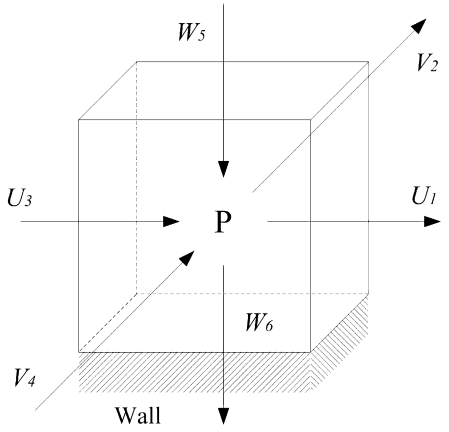


**Fig. 4.** Contravariant velocity distribution of the control volume for 3-D application.

Similarly, the droplet apparent density on the wall boundary cannot be set to be zero, otherwise it is equivalent to a fact that no droplets will impinge onto the wall.

Based on the above analysis and by also taking into account the principle that droplets cannot flow into the interior flowfield from the wall, it is possible to set the wall condition in 2-D application as follows:

If the contravariant velocity $V_P$, located in the center of a control volume near the wall, points to the wall, the droplets within this control volume may impinge onto the wall (as shown in Fig. 3(a)). Then the contravariant velocity on the wall boundary is calculated through an interpolation from the interior flowfield, as is the apparent density on the wall boundary. These contravariant velocity and apparent density are applied as the wall condition for this control volume in the next iteration.

If, however, the contravariant velocity $V_P$ in the center of the control volume near the wall points to the interior flowfield, the droplets have no possibility of impinging on the wall (as shown in Fig. 3(b)). In this case the droplet velocity and apparent density on the wall boundary are set to be zero, which is applied as the wall condition for this control volume in the next iteration.

The setting method of wall conditions in two-dimensional application can be extended into three-dimensional application. Fig. 4 shows the investigated control volume of 3-D application.

The droplet impingement on the airfoil/wing surface can be simulated effectively by applying this kind of wall condition and the accuracy and convergence of numerical computation can also be improved.

### 2.4. Solution of the governing equations for droplets

The unknowns in the droplet governing equations include droplet velocities and apparent density. There are three unknowns for 2-D application and four unknowns for 3-D application. The equations can be solved in closed form because the number of unknowns is equal to the number of equations. The governing equations are discretized using the finite-volume method in body-fitted curvilinear coordinates. The convective term is discretized using QUICK scheme, with the deferred correction method employed. The temporal term is discretized using the first-order implicit scheme.

The droplet apparent density and velocities for 3-D application at time $t^n$ are solutions of

$$J\frac{\bar{\rho}^n-\bar{\rho}^{n-1}}{\Delta t}+\iiint_{\Omega}\left[\frac{\partial}{\partial\xi}(\bar{\rho}U)^n+\frac{\partial}{\partial\eta}(\bar{\rho}V)^n+\frac{\partial}{\partial\zeta}(\bar{\rho}W)^n\right]d\xi\,d\eta\,d\zeta=0 \tag{11}$$

$$J\frac{(\bar{\rho}v_x)^n-(\bar{\rho}v_x)^{n-1}}{\Delta t}+\iiint_{\Omega}\left[\frac{\partial}{\partial\xi}(\bar{\rho}Uv_x)^n+\frac{\partial}{\partial\eta}(\bar{\rho}Vv_x)^n+\frac{\partial}{\partial\zeta}(\bar{\rho}Wv_x)^n\right]d\xi\,d\eta\,d\zeta=\iiint_{\Omega}J\cdot F_{Dx}^n\,d\xi\,d\eta\,d\zeta \tag{12}$$

$$J\frac{(\bar{\rho}v_y)^n-(\bar{\rho}v_y)^{n-1}}{\Delta t}+\iiint_{\Omega}\left[\frac{\partial}{\partial\xi}(\bar{\rho}Uv_y)^n+\frac{\partial}{\partial\eta}(\bar{\rho}Vv_y)^n+\frac{\partial}{\partial\zeta}(\bar{\rho}Wv_y)^n\right]d\xi\,d\eta\,d\zeta=\iiint_{\Omega}J\cdot(F_{Dy}+F_{GB})^n\,d\xi\,d\eta\,d\zeta \tag{13}$$

$$J\frac{(\bar{\rho}v_z)^n-(\bar{\rho}v_z)^{n-1}}{\Delta t}+\iiint_{\Omega}\left[\frac{\partial}{\partial\xi}(\bar{\rho}Uv_z)^n+\frac{\partial}{\partial\eta}(\bar{\rho}Vv_z)^n+\frac{\partial}{\partial\zeta}(\bar{\rho}Wv_z)^n\right]d\xi\,d\eta\,d\zeta=\iiint_{\Omega}J\cdot F_{Dz}^n\,d\xi\,d\eta\,d\zeta \tag{14}$$

where, $\Omega$ is the control volume in body-fitted curvilinear coordinates, $J$ is Jacobi factor and $U$, $V$, $W$ are contravariant velocity components of droplets.

It is worth noting that the possible oscillations in the solution of the governing equations for droplets mentioned in Refs. [2,3] are not found by using the computational method presented in this paper. Therefore, the extra stabilization terms are not needed.

### 2.5. Calculation of collection efficiency

Based on the velocity distribution of airflow, the governing equations for the droplets are solved and the normal velocity $v_{nw}$ and apparent density $\bar{\rho}_w$ of droplets on the wall boundary can be obtained after the numerical computation converges. Therefore, the local collection efficiency $\beta$, which is non-dimensional, can be obtained conveniently with the Eulerian method:

$$\beta=-\alpha\cdot\mathbf{u}\cdot\mathbf{n} \tag{15}$$

where $\alpha$ denotes the value of the ratio of the volume occupied by water over the total volume of the fluid element; $\mathbf{u}$ represents the value of the droplets velocity over the element; and $\mathbf{n}$ expresses the normal direction.

## 3. Boundary layer calculation

### 3.1. Roughness on iced surface

The roughness on iced surface is irregular and its formation mechanism is complex so that it is difficult to simulate the roughness precisely in numerical simulation of ice accretion. The equivalent sand-grain roughness is employed to describe the roughness effect. To a 2-D airfoil, it can be evaluated with the following expression obtained from the experimental data [14]:

$$k_s=0.0008C\cdot(0.047\cdot T_c-11.27)\cdot\left(0.5714+0.2457\cdot LWC+1.2571\cdot LWC^2\right) \tag{16}$$

where $C$ denotes the airfoil chord and $T_c$ denotes the environmental temperature.

### 3.2. Integral boundary layer method

An important parameter in numerical simulation of ice accretion is convective heat transfer coefficient which mainly depends on the property of the boundary layer, such as the momentum thickness, skin friction coefficient, and etc. In this paper, the convective heat transfer coefficient is evaluated through employing an integral boundary layer method based on the ones used in LEWICE [12] and MULTIICE [10] codes.

The roughness Reynolds number is defined as:

$$Re_k=\frac{u_e\cdot k_s}{\upsilon} \tag{17}$$

where, $u_e$ is air velocity at boundary layer edge and $\upsilon$ is kinematic viscosity.

When $Re_k$ is lower than 600, the boundary layer is assumed to be laminar and the momentum thickness can be calculated as:

$$\theta_l=\sqrt{\frac{0.45\upsilon}{u_e^6}\int_0^s u_e^5\,ds} \tag{18}$$

And the convective heat transfer coefficient can be evaluated with the following expression:

$$h_{cv}=\frac{0.293\cdot\lambda\cdot u_e^{1.435}}{\sqrt{\upsilon\cdot\int_0^s u_e^{1.87}\,ds}} \tag{19}$$

where $\lambda$ is air thermal conductivity.

When $Re_k$ is greater than or equal to 600, the boundary layer is thought to be turbulent and the momentum thickness is calculated with the following expression:

$$\theta_t=\frac{0.0263\cdot\upsilon^{0.2}}{u_e^{3.4}}\left(\int_{s_{tr}}^s u_e^4\,ds\right)^{0.8}+\theta_{ltr} \tag{20}$$

where $\theta_{ltr}$ is the laminar momentum thickness at the transition location. Then the convective heat transfer coefficient can be evaluated as:

$$h_{cv}=\rho_a\cdot C_{pa}\cdot u_e\cdot\frac{1/2C_f}{Pr_t+\sqrt{1/2\cdot C_f}\cdot 0.52\cdot(\frac{u_\tau\cdot k_s}{\upsilon})^{0.45}\cdot Pr^{0.8}} \tag{21}$$

where, the symbols $C_{pa}$, $Pr$, $Pr_t$ denote the specific heat of air, Prandtl Number, turbulent Prandtl Number, respectively; and $C_f$, $u_\tau$ denote the skin friction coefficient, friction velocity, respectively. The formulae for evaluating them can be written as follows:

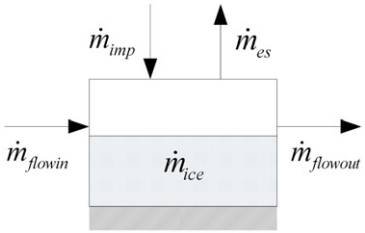


**Fig. 5.** Mass balance in the control volume.

$$1/2C_f = \frac{0.1681}{[\ln(\frac{864\cdot\theta_t}{k_s} + 2.568)]^2} \tag{22}$$

$$u_\tau = u_e \cdot \sqrt{1/2C_f} \tag{23}$$

## 4. Thermodynamic model

The thermodynamic model is based on the classical Messinger model [8] employed by most of the ice accretion codes and the ice amount of every control volume on a 2-D airfoil is evaluated through performing the mass and energy balances.

### 4.1. Mass balance

Fig. 5 shows the mass balance in the control volume on the airfoil.

As shown in this figure, the mass balance equation can be written as:

$$\dot{m}_{imp} + \dot{m}_{flowin} - \dot{m}_{ice} - \dot{m}_{flowout} - \dot{m}_{es} = 0 \tag{24}$$

where $\dot{m}_{imp}$ denotes the impinging water mass in unit time and it can be calculated as:

$$\dot{m}_{imp} = LWC \cdot v_\infty \cdot \beta \cdot A \tag{25}$$

where the symbol $A$ denotes the impingement area of the control volume.

The symbols $\dot{m}_{flowin}$, $\dot{m}_{flowout}$ denote the water mass flowing into the control volume and the one flowing out of control volume in unit time while $\dot{m}_{ice}$, $\dot{m}_{es}$ denote the ice mass and the evaporation or sublimation mass within the control volume in unit time.

The freezing fraction is defined as:

$$f = \frac{\dot{m}_{ice}}{\dot{m}_{imp} + \dot{m}_{flowin} - \dot{m}_{es}} \tag{26}$$

therefore:

$$\begin{aligned} \dot{m}_{ice} &= f \cdot (\dot{m}_{imp} + \dot{m}_{flowin} - \dot{m}_{es}) \\ \dot{m}_{flowout} &= (1-f) \cdot (\dot{m}_{imp} + \dot{m}_{flowin} - \dot{m}_{es}) \end{aligned} \tag{27}$$

### 4.2. Energy balance

The energy transfer within the control volume can be assumed to consist of three parts: the convective heat and impinging heat, latent heat and sensible heat.

#### 4.2.1. Convective heat and impinging heat

The convective heat can be evaluated as:

$$\dot{Q}_{ca} = h_{cv} \cdot (T_{rec} - T_b) \cdot A \tag{28}$$

where the symbols $T_{rec}$, $T_b$ denote the airflow recovery temperature and balance temperature of the control volume.

The impinging heat can be calculated as:

$$\dot{Q}_{imp} = \frac{1}{2}\dot{m}_{imp} \cdot V_{imp}^2 \tag{29}$$

where the symbol $V_{imp}$ is the impinging velocity of droplets obtained from the solution of the droplets' flowfield.

#### 4.2.2. Latent heat

The latent heat of freezing and the one of evaporation or sublimation in unit time can be calculated as follows:

$$\dot{Q}_{freeze} = L_f \cdot f \cdot (\dot{m}_{imp} + \dot{m}_{flowin}) \tag{30}$$

$$\dot{Q}_{es} = -L_{es} \cdot \dot{m}_{es} \tag{31}$$

where the symbols $L_f$, $L_{es}$ denote the latent heat of freezing and evaporation or sublimation per kilogram respectively.

Therefore:

$$\dot{Q}_{latent} = \dot{Q}_{freeze} + \dot{Q}_{es} \tag{32}$$

#### 4.2.3. Sensible heat

The sensible heat occurs with the change of time and temperature. The thermodynamic process of icing in the control volume can be simplified as: the whole input water is first heated up to freezing temperature $T_f$ at which icing phenomenon occurs, then the ice and the water that hasn't been frozen reach the balance temperature $T_b$ finally.

The sensible heat can be calculated as follows:

$$\dot{Q}_{sensible} = \dot{Q}_{simp} + \dot{Q}_{sflowin} + \dot{Q}_{sice} + \dot{Q}_{sflowout} \tag{33}$$

$$\dot{Q}_{simp} = \dot{m}_{imp} \cdot C_{pw} \cdot (T_{imp} - T_f) \tag{34}$$

$$\dot{Q}_{sflowin} = \dot{m}_{flowin} \cdot C_{pw} \cdot (T_{flowin} - T_f) \tag{35}$$

$$\dot{Q}_{sice} = \dot{m}_{ice} \cdot C_{pi} \cdot (T_f - T_b) \tag{36}$$

$$\dot{Q}_{sflowout} = \dot{m}_{flowout} \cdot C_{pw} \cdot (T_f - T_b) \tag{37}$$

where, the symbols $C_{pw}$, $C_{pi}$ denote the specific heat of the water and ice respectively while $T_{imp}$, $T_{flowin}$ denote the droplets' temperature before they impinge onto the airfoil and the temperature of incoming water from the previous control volume.

Therefore, the energy balance equation can be written as:

$$\dot{Q}_{ca} + \dot{Q}_{imp} + \dot{Q}_{lantent} + \dot{Q}_{sensible} = 0 \tag{38}$$

### 4.3. Solution of the mass and energy balances

Substituting Eq. (27) into (38), an equation whose unknowns include $f$ and $T_b$ can be derived and a constraint $f \in [0,1]$ of this equation can be obtained due to the expression $0 \leqslant \dot{m}_{ice} \leqslant (\dot{m}_{imp} + \dot{m}_{flowin} - \dot{m}_{es})$. The computation of this derived equation can be performed from the stagnation point and along the upper and lower airfoil surfaces, respectively, for there is no runback water accepted in the control volumes that the droplets locate at the both sides of the stagnation point. Another assumption is that any runback water flowing out of a control volume will move along the direction away from the stagnation point and in this way the value of $\dot{m}_{flowout}$ in a control volume is equal to the one of $\dot{m}_{flowin}$ in the adjacent downstream control volume.

After the value of $f$ is obtained in every iced control volume on the airfoil, the values of $\dot{m}_{ice}$ and $\dot{m}_{flowout}$ of this control volume can be calculated through substituting $f$ into Eq. (27).

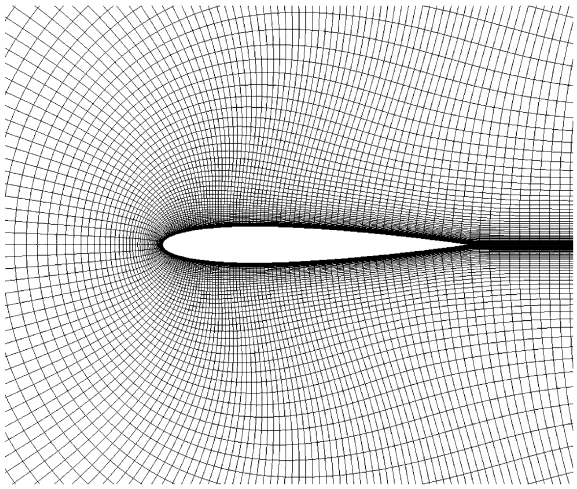

**Fig. 6.** Computational mesh of the clear NACA0012 airfoil.

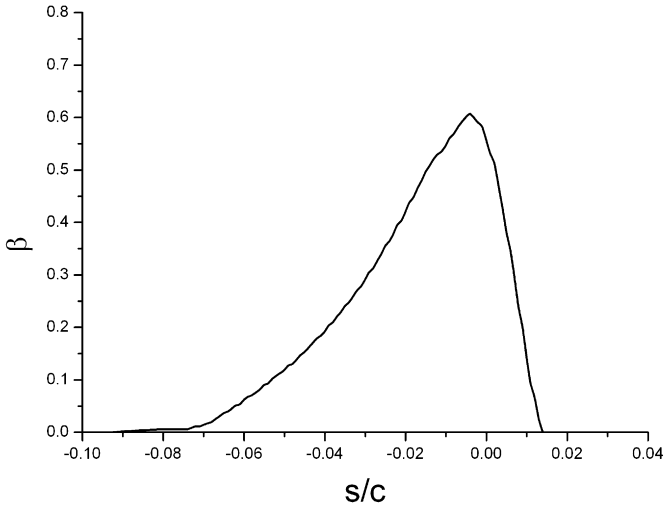


**Fig. 7.** Water collection efficiency of the airfoil at −28.3 °C.

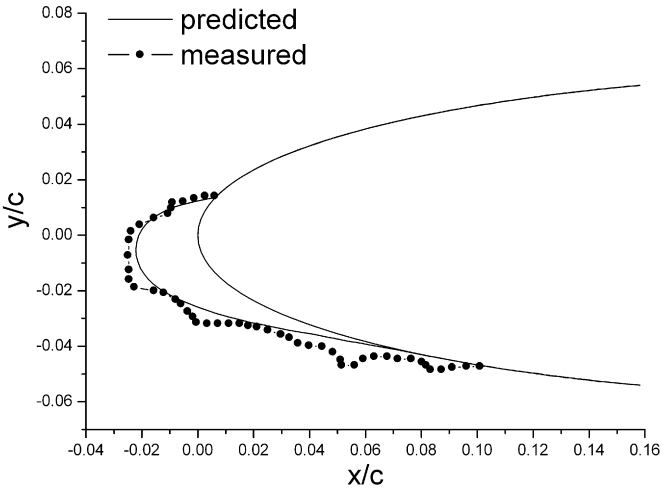


**Fig. 8.** Comparison of ice shapes at −28.3 °C.

## 5. Prediction of ice shape

For 2-D application, the ice amount in every iced control volume can be calculated as:

$$V_{ice} = \frac{\dot{m}_{ice} \cdot \Delta T}{\rho_i} \tag{39}$$

where, $\Delta T$ is time step and $\rho_i$ is ice density.

According to the ice amount, the ice shape after a time step can be built with the assumption that ice grows in the direction normal to the airfoil surface. It should be noted that when the shape of the airfoil is changed by ice accretion, the air flowfield is changed together with it. Therefore, the air flowfield needs to be re-solved, so do the governing equations for droplets. The collection efficiency is then re-calculated. The ice amount is re-evaluated through the thermodynamic model and the new ice shape can be built according to this process. The final shape of ice accretion can be obtained by repeating these steps until the end of ice accretion time.

For 3-D application, the rime ice accretion is simulated using an assumption that the supercooled droplets freeze immediately when they impinge onto the wing surface. Since the rime ice accretion forms in an environment with a low temperature, this assumption is reasonable. In 3-D application, therefore, the ice amount can be calculated as:

$$V_{ice} = \frac{LWC \cdot v_\infty \cdot \beta \cdot A' \cdot \Delta T}{\rho_i} \tag{40}$$

where the symbol $A'$ denotes the impingement area of a 3-D control volume.

## 6. Results and analysis

This paper investigates the ice accretions on a NACA0012 airfoil for 2-D application and on a GLC-305 wing model for 3-D application.

### 6.1. Ice accretion prediction for two-dimensional application

Fig. 6 shows the computational mesh of the clear NACA0012 airfoil.

The computational conditions are: the angle of attack $\alpha = 4°$, the velocity of free stream $u_\infty = 67.05$ m/s, the pressure $p_\infty = 101300$ Pa, the liquid water content $LWC = 1.0$ g/m$^3$, the median volumetric diameter $MVD = 20$ μm and ice accretion time is selected to be 360 seconds.

Fig. 7 shows the water collection efficiency of the airfoil at −28.3 °C.

Figs. 8, 9, 10 show the comparisons between the predicted results and experimental data [14] at different environmental temperatures.

In Fig. 8, the environmental temperature is low enough (−28.3 °C) to make the droplets freeze immediately at their impinging location and the predicted ice shape shows the obvious characteristics of the rime ice accretion. In Fig. 9, the environmental temperature is higher (−13.34 °C) and the predicted ice shape has characteristics of the mixed ice accretion. In Fig. 10, the typical glaze ice accretion is predicted because of the high environmental temperature (−6.1 °C). From the comparisons between the predicted results and the measured ones in Figs. 8, 9, 10, some fairly good agreements could be found.

### 6.2. Ice accretion prediction for three-dimensional application

Fig. 11 shows the geometrical outline of the GLC-305 wing model [9]. Fig. 12 shows the mesh distribution on the wing surface.

The computational conditions are: the velocity of free stream $u_\infty = 89.97$ m/s, the pressure $p_\infty = 61\,282$ Pa, the liquid water

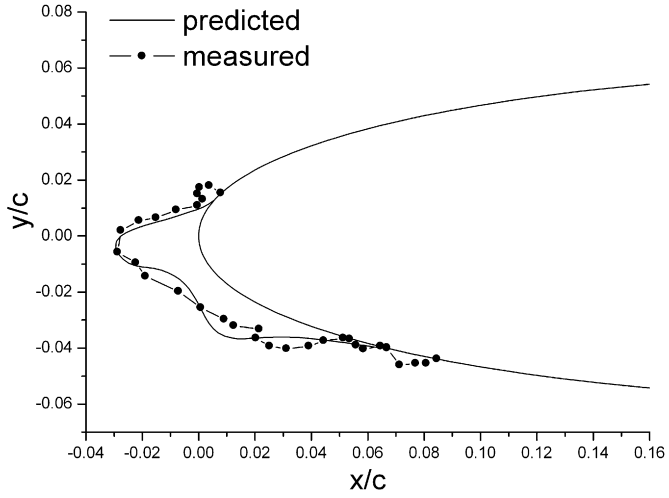


**Fig. 9.** Comparison of ice shapes at −13.34 °C.

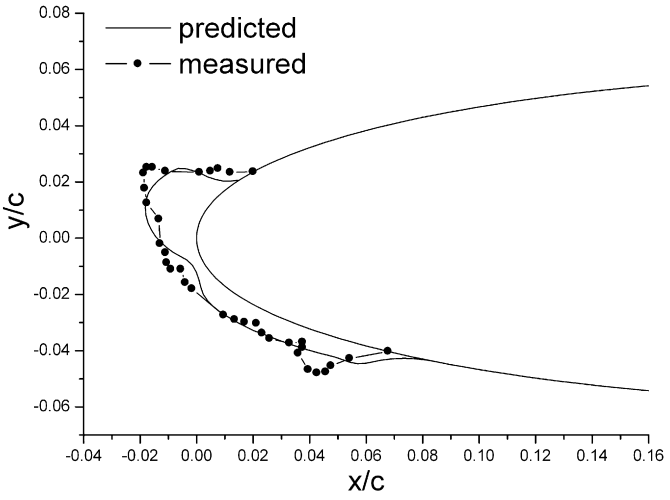


**Fig. 10.** Comparison of ice shapes at −6.1 °C.

content $LWC = 0.51$ g/m$^3$, the median volumetric diameter $MVD =$ 14.5 μm and ice accretion time is selected to be 300 seconds.

Figs. 13(a), (b) show the distributions of local collection efficiency on the wing at 0° and 6° angles of attack respectively.

Fig. 14 shows the predicted ice accretion shapes at 0° and 6° angles of attack, respectively.

From Figs. 13(a) and 14(a), it can be seen that at 0° angle of attack the distribution of the local collection efficiencies and the predicted ice shapes on the lower and upper wing surface are almost symmetrical. When the angle of attack is equal to 6° (in Figs. 13(b) and 14(b)), the main impingement region of the droplets moves to the lower surface of the wing and the ice accretion is mostly found on the lower surface accordingly.

From Fig. 13, the collection efficiency in the wingtip region is larger than in the other region on the wing at both 0° and 6° angles of attack due to the sweep effect of the wing. This phenomenon is consistent with the computational result in Ref. [3]. As for the predicted results of the 3-D rime ice accretion, from Figs. 15(a) to (c), as compared with the experimental results and LEWICE results, the present results are in a good agreement with them. Moreover, from Figs. 15(a) to (c), the thickness of the ice accretion decreases, and this phenomenon agrees with variation of the collection efficiency.

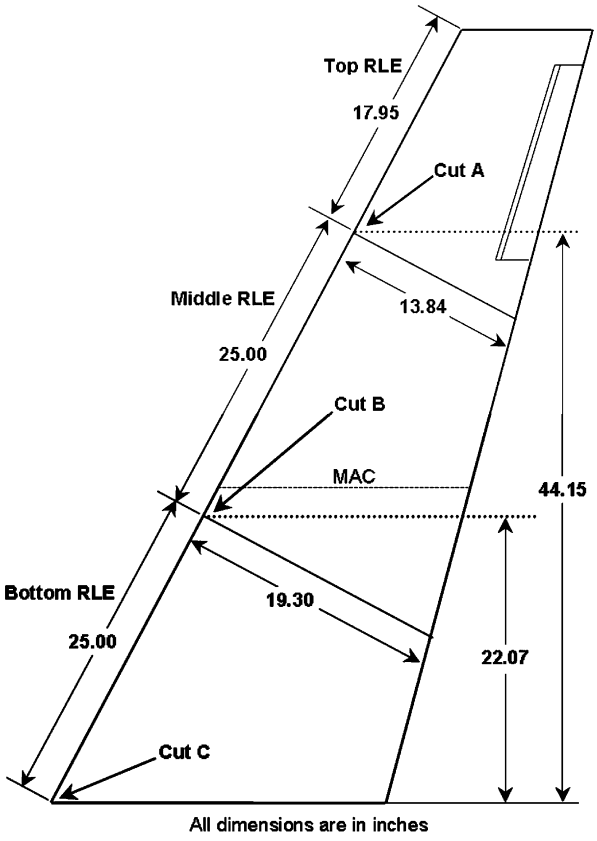


**Fig. 11.** Geometrical outline of the GLC-305 wing model.

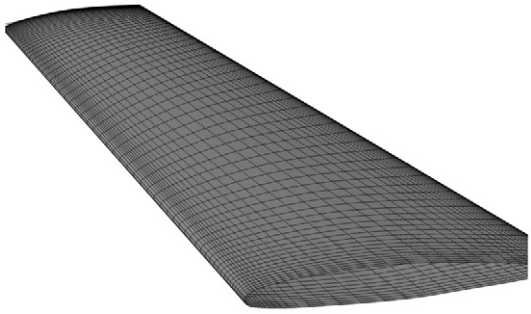

**Fig. 12.** Mesh distribution on the GLC-305 wing model.

## 7. Conclusions

A numerical simulation method to predict the ice accretions on a 2-D airfoil and a 3-D wing is presented based on the Eulerian two-phase flow theory. Several conclusions can be drawn through investigating the ice accretions on a NACA0012 airfoil and a GLC-305 wing model:

(1) The permeable wall proposed in this paper could simulate the droplet impingement on the iced surface effectively and it is convenient to obtain the collection efficiency through applying this wall condition into the numerical computation of the droplet flowfield.
(2) The convective heat transfer coefficient on iced surface is evaluated through employing an integral boundary layer method modified to consider the roughness effect so that the solution of complete N-S equations can be avoided. The thermodynamic model which is based on the classical Messinger model could simulate the icing process while this model is relatively brief.

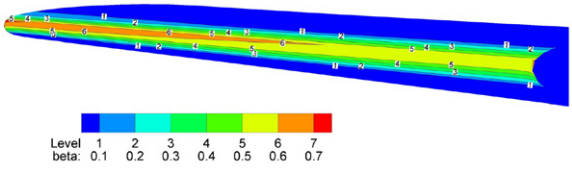


(a) 0° angle of attack.

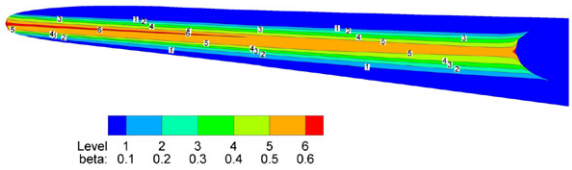


(b) 6° angle of attack.

**Fig. 13.** Distribution of local collection efficiency on the wing at 0° and 6° angle of attack.

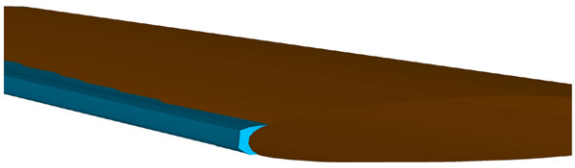

(a) Ice accretion shape at 0° angle of attack.

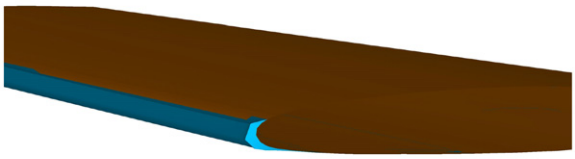

(b) Ice accretion shape at 6° angle of attack.

**Fig. 14.** Predicted ice accretion shape at 0° and 6° angle of attack.

(3) Ice accretions corrupt the designed aerodynamic shapes of the airfoil and wing. There are different ice shapes in different conditions, and the corruption of aerodynamic shapes caused by glaze ice is more severe than that of rime ice. Moreover the ice accretion of NASA 0012 airfoil and the GLC-305 wing model are simulated through the calculation, and the results are reasonable and feasible.

## Acknowledgements

This work is supported by Aeronautical Science Foundation of China (2009ZA51007).

## References

[1] H.E. Addy, M.G.J. Potapczuk, D.W. Sheldon, Modern airfoil ice accretions, AIAA paper 1997-0174.
[2] H. Beaugendre, F. Morency, W.G. Habashi, FENSAP-ICE's three-dimensional in-flight ice accretion module: ICE3D, J. Aircraft 40 (2) (2003) 239–247.

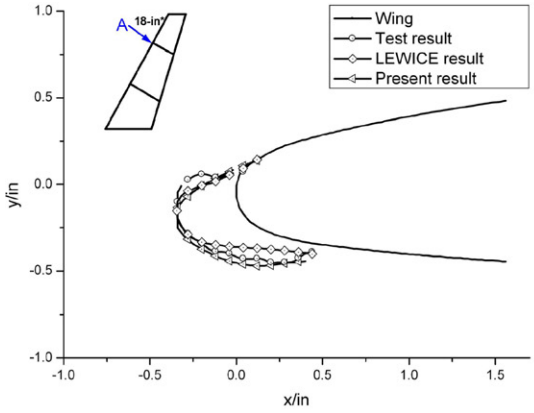


(a) Comparison of ice shape in station A.

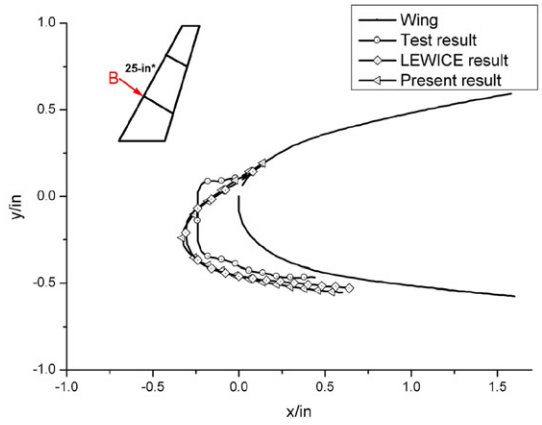


(b) Comparison of ice shape in station B.

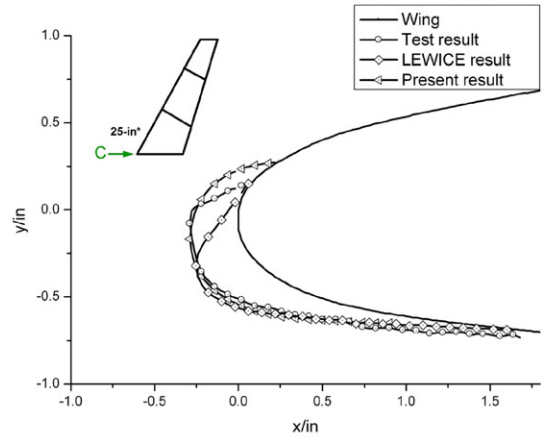


(c) Comparison of ice shape in station C.

**Fig. 15.** Predicted ice accretion shape at 6° angle of attack.

[3] Y. Bourgault, W.G. Habashi, J. Dompierre, Z. Boutanios, An Eulerian approach to supercooled droplets impingement calculations, AIAA paper 1997-0176.
[4] D.T. Bowden, A.G. Gensemer, C.A. Sheen, Engineering summary of airframe icing technical data, FAA Technical Report ADS-4, 1963.
[5] R.W. Gent, TRAJICE2–A combined water droplet trajectory and ice accretion prediction program for aerofoils, RAE TR 90054, 1990.
[6] T. Hedde, D. Guffond, ONERA three-dimensional icing model, AIAA J. 33 (6) (1995) 1038–1045.
[7] E. Iuliano, V. Brandi, G. Mingione, C. de Nicola, R. Tognaccini, Water impingement prediction on multi-element airfoils by means of Eulerian and Lagrangian approach with viscous and inviscid air flow, in: Proceedings of 44th AIAA Aerospace Sciences Meeting and Exhibit, Reno, NV, January 2006.
[8] B.L. Messinger, Equilibrium temperature of an unheated icing surface as a function of air speed, J. Aeronaut. Sci. 20 (1) (1953) 29–42.

[9] Michael Papadakis, Hsiung-Wei Yeong, See-Cheuk Wong, Mario Vargas, Mark G. Potapczuk, Aerodynamic performance of a swept wing with ice accretions, AIAA 2003-0731.
[10] G. Mingione, V. Brandi, B. Esposito, Ice accretion prediction on multi-element airfoils, AIAA paper 1997-0177.
[11] I. Parachivoiu, F. Saeed, Aircraft Icing, A Wiky-Interscience Publication, John Wiley & Sons, Inc.
[12] G.A. Ruff, B.M. Berkowitz, User's manual for the NASA Lewis ice accretion prediction code (LEWICE), NASA CR 185129, 1990.
[13] J. Shin, T.H. Bond, Results of an icing test on a NACA 0012 airfoil in the NASA Lewis Icing Research Tunnel, AIAA paper 1992-0647.
[14] J. Shin, T.H. Bond, Experimental and computational ice shapes and resulting drag increase for a NACA 0012 airfoil [R], NASA TM 105743, 1992.
[15] M. Snellen, O.J. Boelens, H.W.M. Hoeijmakers, A computational method for numerically simulating ice accretion, AIAA paper 1997-2206.
[16] K. Tsuboi, Numerical simulation of ice accretion on a body with droplet flow Model, AIAA paper 1999-3333.
[17] R.W. Wilder, A theoretical and experimental means to predict ice accretion shapes for evaluation aircraft handling and performance characteristics, Paper 5, AGARD Advisory Report No. 127, 1977.
[18] L.X. Zhou, Theory and Numerical Modeling of Turbulent Gas-Particle Flows and Combustion, Science Press and CRC Press, New York, 1993.